OPEN ACCESS
Vol 5, No. 1, 2018, 115-130

Geoplanning
Journal of Geomatics and Planning
E-ISSN: 2355-6544
http://ejournal.undip.ac.id/index.php/geoplanning
doi: 10.14710/geoplanning.5.1.115-130

APPLICATION OF UAV WITH FISH-EYE LENSES CAMERA FOR 3D SURFACE MODEL RECONSTRUCTION

N. Purwono [a], A. Syetiawan [a]

[a] *Geospatial Information Agency of Indonesia*

Article Info:
Received: 01 August 2017
in revised form: 10 Dec 2017
Accepted: 30 January 2018
Available Online: 30 April 2018

Keywords:
UAV, Fish-eye lenses, image processing, 3D surface model, model accuracy

Corresponding Author:
Nugroho Purwono
Geospatial Information Agency of Indonesia
Email: Inugpurwono@gmail.com

Abstract: *Application of Unmanned Aerial Vehicles (UAV) for images acquisiton has been widely applied in survey and mapping. One of non-metric camera as the sensor that can be mounted on the UAV is fish-eye lenses. Fish-eye lenses camera provides images with wide range coverage. However these images are distorted and make them more difficult to use for mapping or 3D modelling. This research is aimed to make a 3D surface model by images reconstruction and to estimate the geolocation accuracy of the model generated by UAV images processing. As the approach of the method, combines the automation of computer vision technique with the photogrammetric grade accuracy. The complete photogrammetric workflow implemented in Pix4D Mapper. Meanwhile, UAV platform used is DJI Phantom 2 Vision+. Sample location in this research is an area of Geospatial Laboratorium in Parangtritis, Yogyakarta. The covered area in this research is 3.934 Ha. From the results of 186 images obtained 2.47 cm value of average Ground Sampling Distance (GSD). Moreover the numbers of 3D points for Bundle Block Images Adjustment are 243,373 points with 0.4348 value of Mean Reprojection Error (pixels). The results of 3D Densified Points are 6,207,780 and 101.04 points of average density per-m3. Generally, geolocation acuracy of the model produced by using this method is between 2.47 - 4.94 cm. Thus, it can be concluded that UAV with fish-eye lenses camera can be used to reconstruct 3D surface model. However, images correction and calibration should be required to produce an accurate 3D model.*

How to cite (APA 6th style): Purwono, N., & Syetiawan. (2018). Application of UAV with fish-eye lenses camera for 3D surface model reconstruction. *Geoplanning: Journal of Geomatics and Planning, 5*(1), 115-130. doi: 10.14710/geoplanning.5.1.115-130

1. INTRODUCTION

Unmanned Aereial Vehicle or UAV becomes more popular and extensively applied in various field of practical applications (Azmi et al., 2014; Bemis et al., 2014; Han et al., 2013). The use of UAV is suitable for survey and mapping (Clapuyt et al., 2016). UAV is one of the alternative ways to ease the process of acquiring data (Azmi et al., 2014), with lower operating and manufacturing cost (Nex & Remondino, 2013). Furthermore, UAV platforms are valuable source for inspection, surface monitoring, mapping and 3D modelling (Nex & Remondino, 2013). In mapping and 3D modelling, an accurate and high-resolution images as representation of the earth surface is required (Clapuyt et al., 2016). As one of the alternative and efficient ways to produce high-resolution images, UAV is capable to performing those due to improving aerial photogrammetry aspect (Nex & Remondino, 2013).

Several years ago, aerial photogrammetry technology continues to grow, both in terms of data collecting and processing (Colomina & Molina, 2014). As well as development of light aerial photogrammetry platforms such as UAV's cameras. However, UAV has some limitations due to the suitability of its camera as the sensor. For instance, to build a surface model by using UAV has limitation on large-scope mapping area, that is related to camera as measurement tool (Eisenbeiß et al., 2009). In addition to any limitations of that platform, UAV brings new oportunities to provide an alternative method in mapping (Cook, 2017; Eisenbeiß et al., 2009; Kršák et al., 2016).

The use of the camera is a main component of image data capturing for aerial photogrametry like small-light UAV in particular (Clapuyt et al., 2016; Nex & Remondino, 2013; Wang & Li, 2008). According to (Gularso et al., 2015), for the small area (<100 ha) aerial photogrammetry using metric camera is not efficient, because the operational cost incurred is not comparable with a small volume of work. Non metric

camera through small format standard camera can be used as an alternative method, this method is known as Small Format Aerial Photography (SFAP) (Aber et al., 2010). However, SFAP leads to new problems due to small light-weight construction of their platform, such as higher agility and more susceptibility to turbulence, which has big impact on the quality of the data and their suitability for aerial photography (Gurtner et al., 2009).

As the Small Format Aerial Photography (SFAP), there are various kinds of non-metric cameras that commonly mounted on their platforms. One of them is fish-eye lenses camera. A fish-eye lenses is a wide-angle lenses that produces strong visual distortion intended to create wide panoramic or hemispherical image. These fish-eye lenses have advantages relate to the efficiency in data capture, as the processing is highly automated, contributes dominantly to the total cost of terrestrial or indoor surveying (C. Strecha et al., 2014). The disadvantage of fish-eye lenses is their large and very non-uniform ground sampling distance (GSD), when compared to perspective lenses (Schneider et al., 2009; C. Strecha et al., 2014).

Fish-eye lenses is rarely used in 3D surface modeling due to its distortions and errors (Luhmann et al ., Fraser, & Maas, 2016; Schneider et al., 2009; Schwalbe, 2005). This kind of lenses is different from the others because it has convex distortion effect on the produced objects. It is hemispherical(see Figure 1), and has wide angle (C. Strecha et al., 2014). Therefore, wider range of this lenses has several limitations to make surface models (Schneider et al., 2009; Schwalbe, 2005).

Figure 1. Sample of hemispherical image of fish-eye lenses captured

In aerial photogrametry, to generate a surface model such as Digital Surface or Terrain Model (DSM/DTM) use conventional or central perspective lenses camera to perform photogrammetric data acquisition (Bemis et al., 2014; Kršák et al., 2016; Nex & Remondino, 2013; Remondino et al., 2012). The result of used of standart cameras is indicating inherently multidimensional (x, y, z, point orientation, colour, texture), archival and easily transformed into orthorectified photomosaics or Digital Elevation Models (DEMs) (Bemis et al., 2014). Moreover, by using that technology is suitable to form 3D models in detail and accurately (Kršák et al., 2016). Therefore, 3D results like DSM/DTM, contour lines, textured 3D models, vector data, etc. can be produced, in a reasonable way (Remondino et al., 2012). On the other hand, fish-eye lenses technology offer an alternative way to performs photogrammetric data acquisition. It provides more flexibility for images capturing. For example, advantageously provide images with wide coverage; however, these images are extremely distorted and their non-uniform resolutions make them

more difficult to use for mapping or terrestrial 3D modelling (Strecha et al., 2014). Despite mathematical model for fish-eye lenses camera systems was developed, implemented and tested (Luhmann et al., 2016; Schneider et al., 2009). The model for fish-eye lenses camera deviates from the conventional or central perspective camera model by introducing spherical coordinates (Kannala & Brandt, 2006). This means that a ray in object space is described by its azimuth and its inclination angle (Kannala & Brandt, 2006; Schneider et al., 2009). In order to adapt to the physical reality, the model is extended by additional parameters to make a representative model (Kannala & Brandt, 2006; Schneider et al., 2009; Schwalbe, 2005; C. Strecha et al., 2014).

Generally, the conventional or central perspective camera is used to make terrestrial or 3D surface models. Therefore, the use of fish-eye lenses in mapping will be different oportunities in particular to produce 3D surface models. This research focused on the application of fish-eye lenses to produce 3D surface models. This study aims to exam the use of fish-eye lenses mounted on UAV for 3D surface modeling by images reconstruction. This paper describe a detailed investigation from the fish-eye lenses distortion to the registering of the images and estimate the geolocation accuracy of the model generated through UAV images processing autonomously.

2. DATA AND METHODS

Location in this research is an area of Parangtritis Geomaritime Science Park (PGSP), Yogyakarta with 3.934 Ha covered area. The images are taken from 87.8 meters above the ground and average speed of UAV's is 10 m/s. In accordance with government regulations about UAV controlling which are issued by Ministry of Transportation, stated that the highest fly point of UAV allowed is 150 m¬eters above ground. There are several steps to take images in this research (Figure 2). The first step is to determine the flight plan in accordance with Area of Interest (AOI). The next step is to take the images (aerial image acquisition) and then continued by automatic image processing to produce 3D surface models.

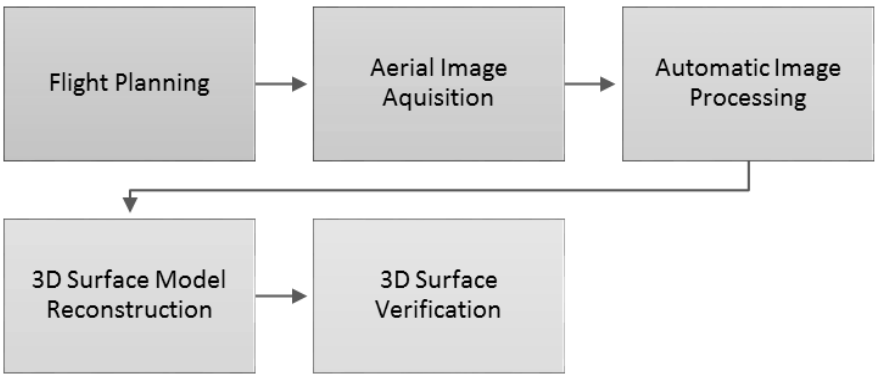

Figure 2. Workflow of this method

2.1. Platform and Sensor

UAV platform in this research used DJI Phantom 2 Vision+ (see Figure 3). As a kind of small-light UAV, DJI Phantom 2 vision+ is quad copter type with many configurations which can be controlled by the usser. DJI Phantom 2 Vision+ completed with a set of GPS which can be used in auto-pilot mode. DJI Phantom 2 Vision+ has RGB sensor and fish-eye lenses type so that it can generate a very high resolution of images. Different from fixed wing type, this type can take off and landing vertically everywhere without runway (Nex & Remondino, 2013; Remondino et al., 2012). Table 1 shows the specification of DJI phantom 2 version+.

Figure 3. DJI phantom 2 vision+

Table 1. Specification DJI phantom 2 vision+ (Source: www.dji.com)

Item	Specification
I. Aircraft	
1. Weight (Battery & Propellers included)	1242g
2. Max Flight Speed	15 m/s (not recommended)
3. Diagonal motor-motor distance	350 mm
II. Camera	
1. Sensor size	1/2.3" = 6.17mm x 4.55mm
2. Effective Pixels	14 MP
3. Resolution	4384 x 3288
4. Focal lenght	5 mm
5. Recording FOV	110°/85°
III. Other	
1. Operating frequency	2412-2462 MHz
2. Communication distance (open area)	500-700m
3. Power Consumption	2W

2.2. Fish-eye projection model

The fish-eye projection is based on the principle that in the ideal case the distance between an image point and the principle point is linearly dependent on the angle of incidence of the ray from the corresponding object point (Schneider et al., 2009; Schwalbe, 2005)(see Figure 4). Thus the incoming object ray is refracted in direction of the optical axis. This is realised by the types and the configuration of the lenseses of a fish-eye lenses system (Schwalbe, 2005).

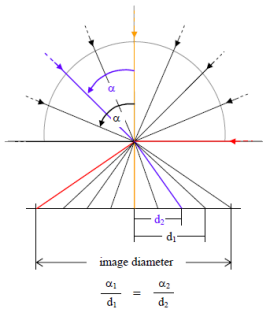

Where:
α = angle of incidence
d = distance between the ray and the optical axis

Figure 4. Fish-eye projection model (Souce: Schwalbe, 2015)

To reconstruct the projection of an object point into the hemispherical image, the object coordinates and image coordinates have to refer to the same coordinate system. Therefore, first the object coordinates which are known in the superior coordinate system have to be transformed into the camera coordinate system with the following transformation equations (Schwalbe, 2005).

$$Xc = r11 . (X - X0) + r21 (Y - Y0) + r31 (Z - Z0) \quad (1)$$
$$Yc = r12 . (X - X0) + r22 (Y - Y0) + r32 (Z - Z0) \quad (2)$$
$$Zc = r13 . (X - X0) + r23 (Y - Y0) + r33 (Z - Z0) \quad (3)$$

Where:
XC, YC, ZC = object point coordinates in the camera coordinate system
X, Y, Z = object point coordinates in the object coordinate system
X0, Y0, Z0 = coordinates of the projection centre
rij = elements of the rotation matrix

2.3. Image Processing

The complete photogrammetric workflow as image processing is implemented in commercial software (Pix4D-mapper). Pix4D-mapper is designed to process aerial imageries, and offers viewing, editing and annotating features automatically (Strecha, 2011). It software is also used to produce surface model from complex structure using aerial imageries (Niederheiser et al., 2016; Strecha, 2011). The software supports both standard perspective camera models and equidistant fish-eye camera models (Niederheiser et al., 2016; Strecha et al., 2014; Strecha, 2011). Given the world coordinates (X,Y,Z) in the camera centric coordinate system, the angle θ between the incident ray and the camera direction is given by (Strecha et al., 2014):

$$\theta = \frac{2}{\pi}\arctan\left(\frac{\sqrt{X^2+Y^2}}{Z}\right) \quad (4)$$

The angle θ is then further modeled by the polynomial coefficient pi, which is part of the camera model:

$$\rho = p_0+\theta + p_2\,\theta^2 + p_2\,\theta^3 \quad (5)$$

The projection of the world coordinates into image pixel coordinates (x, y) is then given by:

$$X_h = \frac{\rho X}{\sqrt{X^2+Y^2}} \quad , \quad Y_h = \frac{\rho Y}{\sqrt{X^2+Y^2}} \quad (6)$$

$$\begin{pmatrix} x \\ y \end{pmatrix} = \begin{pmatrix} c & d \\ e & f \end{pmatrix} \begin{pmatrix} Xh \\ Yh \end{pmatrix} + \begin{pmatrix} c_x \\ c_y \end{pmatrix} \quad (7)$$

with the affine transformation parameters (c,d,e,f,cx,cy). Note that (c, f) indicates the focal length and (cx, cy) is the principal point coordinate in image space. The polynomial coefficient $p1$ is redundant to the parameters (c, f) and are defined to be 1 (see Figure 5)

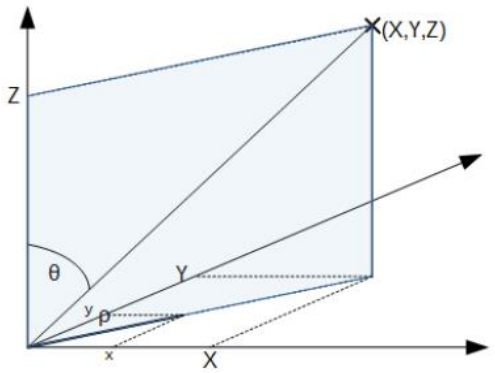

Figure 5. Geometric model of a fish-eye lenses as formulated in Equations 4-7 (Source: Strecha et al., 2014)

2.3.1. Camera self calibration

This process optimizes internal camera parameters, such as focal length, principal point auto collimation, lenses distortions and etc. Trough the Pix4D-mapper, the camera interior parameters was calibrated from datasets. Distributed tie points are found and measured on overlapped images and then

used to optimize the parameters. Once the parameters are obtained, they are stored in the Pix4D-mapper camera database. The method is also known as the self-calibration bundle adjustment. Whenever a new project is created, the algoritm searches for matched models and brings in the camera interior parameters, which are already calibrated, and later on there's the possibility to re-calibrate them using the current dataset (Strecha et al., 2014). Table 2 shows the specification of DJI phantom 2 version+.

Table 2. Example of camera self calibration result

Image	Group	Latitude (degree)	Longitude (degree)	Atitude (m)	Accuracy Horz (m)	Accuracy Vert (m)	Omega (degree)	Phi (degree)	Kappa (degree)
DJI00826.JPG	group1	-8.0088306	110.3013667	49.287	5.000	10.000	2.13974	6.59292	71.97408
DJI00827.JPG	group1	-8.0087917	110.3014583	49.861	5.000	10.000	0.07909	-2.15855	-87.90118
DJI00828.JPG	group1	-8.0088056	110.3015528	50.525	5.000	10.000	0.13854	-3.77746	-87.89812
DJI00829.JPG	group1	-8.0088278	110.3016444	49.376	5.000	10.000	0.06384	-3.32939	-88.90084
DJI00830.JPG	group1	-8.0088500	110.3017389	49.130	5.000	10.000	-0.24634	-2.86945	-94.90888
DJI00831.JPG	group1	-8.0088472	110.3018389	49.235	5.000	10.000	0.11676	-2.15684	-86.90053
DJI00832.JPG	group1	-8.0088333	110.3019389	49.300	5.000	10.000	0.09156	-4.76912	-88.89892
DJI00833.JPG	group1	-8.0088306	110.3020333	49.329	5.000	10.000	0.01167	-6.83999	-89.90205
DJI00834.JPG	group1	-8.0088333	110.3021333	49.879	5.000	10.000	0.00981	-5.75999	-89.90227
DJI00835.JPG	group1	-8.0088444	110.3022333	48.752	5.000	10.000	-0.14972	-4.49751	-91.90866
DJI00836.JPG	group1	-8.0088500	110.3023444	49.324	5.000	10.000	0.07249	-3.77931	-88.90040
DJI00837.JPG	group1	-8.0088389	110.3024361	50.277	5.000	10.000	-0.06392	-4.04950	-90.90507
DJI00838.JPG	group1	-8.0088250	110.3025306	49.852	5.000	10.000	0.25150	-6.83540	-87.88780

2.3.2. Automated aerial-image triangulation and bundle block adjusment

Aerial-image triangulation is one of the key processes in digital photogrammetric production which has the highest potential for automation and efficiency (Eisenbeiß et al., 2009; Gini et al., 2013; Kersten et al., 1997). While image processing and computer vision techniques have successfully been employed for facilitating automated procedures in digital aerial-image such as interior orientation (Gini et al., 2013; Kersten et al., 1997; Niederheiser et al., 2016), relative orientation, point transfer in photogrammetric block triangulation, and the generation of Digital Surface Models (Kršák et al., 2016; Nex & Remondino, 2013; Remondino et al., 2012).

Trough the Pix4D-mapper, process automatically with or without known camera position and exterior orientation. The number of automatic tie points on all images that are used for the automatic aerial triangulation and bundle block adjustment. It corresponds to the number of all keypoints or characteristic points that could be matched on at least two images. The number of all 3D points that have been generated by matching 2D points on the images. Each computed 3D point has initially been detected on the images. On each image detected 2D keypoint has a specific position. When computed 3D point is projected back to the images it has a re-projected position. The distance between the initial position and the re-projected position one gives a re-projection error (Figure 6). Considered by Figure 7, the re-projection error is the distance between the marked and the re-projected point. It is a good indication of a successful or not reconstruction of the model.

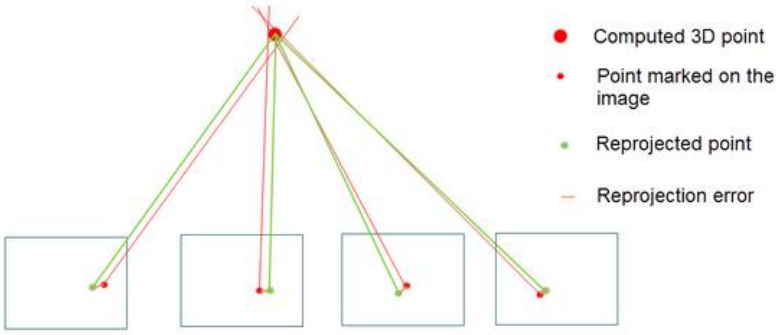

Figure 6. Re-projection error

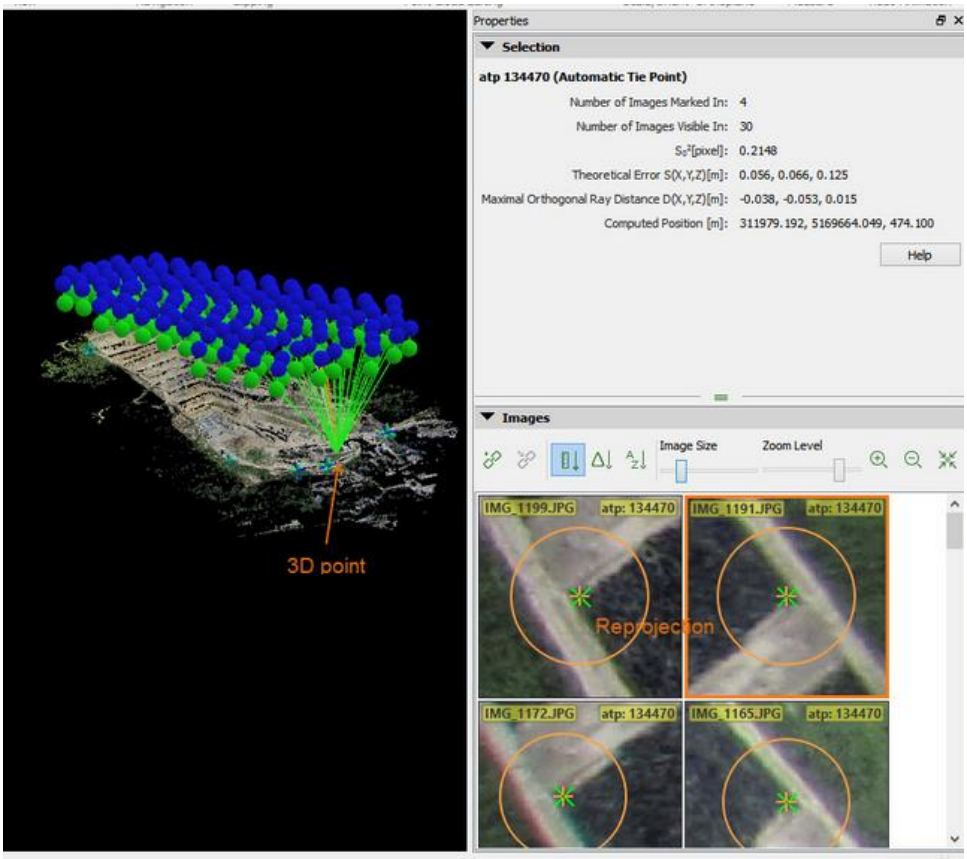

Figure 7. 3D Point re-projection

2.3.3. Automated point cloud densification and classification

The matched point correspondences are evaluated with parameters from the optimization in order to keep good matches and discard bad ones (Bandara et al., 2011; Clapuyt et al., 2016; Niederheiser et al., 2016). The purpose is to find details close to a plane in the images, or on plane-like surfaces. The Point Density has an impact on the number of 3D points generated. Trough the Pix4D algorithm, 3D points are computed on multiple image scales. The 3D points are computed on images with half, quarter and eighth image size. This is useful for computing additional 3D points in vegetation areas as well as keeping details in areas without vegetation. This research used a 3D points computed for every 4/image scale pixel. For example, if the image scale is set to 1/2 or half image size, one 3D point is computed every 4/0.5 = 8 pixels of the original image.

2.3.4. Orthomosaic generation

The orthomosaic generation is based on orthorectification. This method removes the perspective distortions from the images using the 3D model (Clapuyt et al., 2016; Nex & Remondino, 2013; Remondino et al., 2012; Strecha et al., 2014). A high number of matches/keypoints or more than 1000 is required to

generate the 3D model. This method handles all types of terrain, as well as large datasets. Distances are preserved and therefore the orthomosaic can be used for measurements. Number of overlapping images computed for each pixel of the orthomosaic (Figure 8). Red and yellow areas indicate low overlap for which poor results may be generated. Green areas indicate an overlap of over 5 images for every pixel. Good quality results will be generated as long as the number of key point matches is also sufficient for these areas.

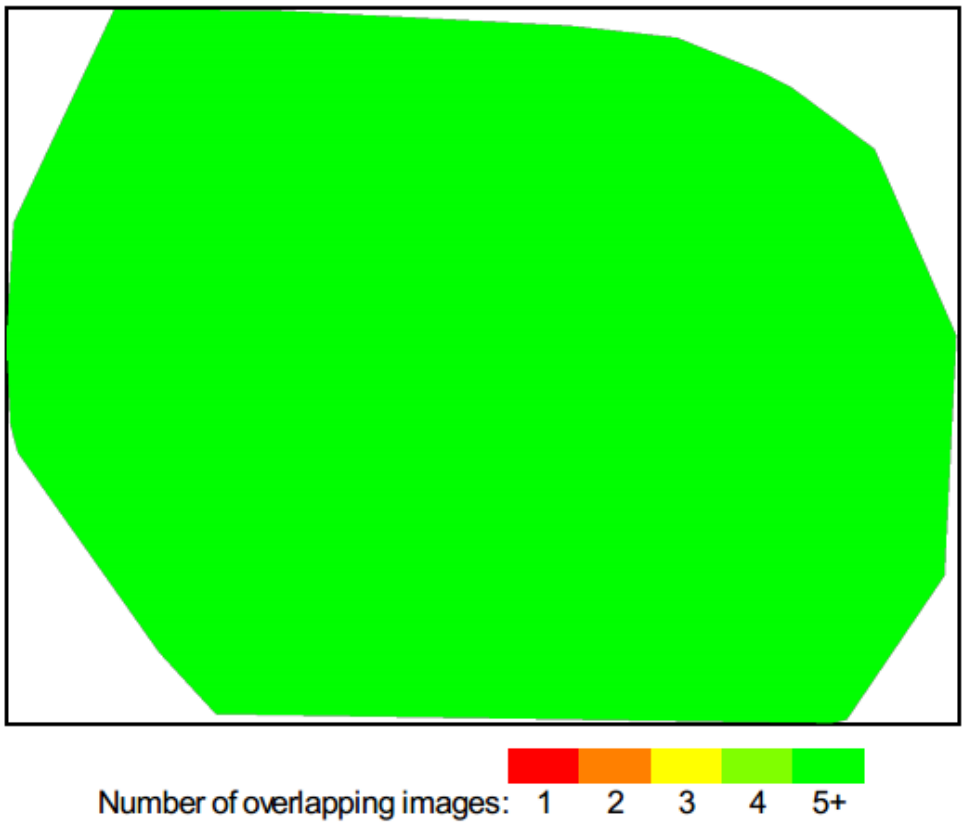

Figure 8. Number of overlapping images for each pixel of the orthomosaic

3. RESULTS AND DISCUSSION

In this case, the images are taken automatically by the UAV according to the selected images acquisition plan without any intervention. Starting from the covered area, UAV flight plan can be shown as Figure 9. The covered area in this research is 3,934 Ha.

Figure 9. Image aqusition plan / flight plan

3.1. Ground Sample Distance and Images Acquisition

To formalising surface model by using image reconstrucion, one of the most important parameter is Ground Sample Distance (GSD) (Felipe-Garc'ia et al., 2012). The GSD is the distance between two consecutive pixel centers measured on the ground. It mean the lower value of GSD, the higher the spatial resolution of the images and the more visible details. In this research, by using a camera with a real focal length (FR) of 5 mm, a real sensor width (Sw) of 6.17 mm, and the image width (imW) of 4384 pixels. Assuming that the flight height is 87.8 m and using the equation (8), the result of computation of the average GSD should be 1.43 cm/pixel.

$$H = (imW * GSD * FR) / (Sw * 100) \quad (8)$$

Even when flying at a constant height, the result on each image may not have the same GSD. This is due to terrain elevation differences and changes in the angle of the camera while shooting. Since the orthomosaic is created using the 3D point cloud and the camera positions, an average GSD will be computed and used. In this research, the result achieved with the average GSD value based on maximum and minimum ground elevations per-image. It is also presented as well as the base/height ratios achieved on normal over surface model.

The flight plans are linear with fly-way with the camera tilting of 90°. Based on UAV flight plan, 186 images were captured by the camera for a dataset. The Result of dataset were explain that 180 (96%) out of 186 images were calibrated into 3 blocks. It means almost all images are enabled. A median of 42833 keypoints per images are found. After matching process, median of 2912.92 matches per-calibrated image. Thus, with the result that the fisheye lens projection follows an approximately linear relation between the incidence angle of an object points beam and the distance from the corresponding image point to the principle point (Kannala & Brandt, 2006; Luhmann et al., 2016; Schwalbe, 2005).

3.2. Images Processing and Bundle Block Adjustment Details

By using Pix4D-mapper, in particular to images processing with editing and annotating features was performed automatically. Trough the Pix4D algorithm, images points are computed on multiple image scales. The spatial resection results of the images will be verified in a bundle adjustment procedure with a

total of images taken in the same calibration. In particular, caused by the accuracy of reference points leads to an improvement of the adjustment precision parameters in comparison to the spatial resection results. The images constellation of used positions by keypoint matches is shown in Figure 11. Thereby the camera axes were oriented convergent in a way that a maximal number of object points are visible within the image. Furthermore, it shows that number of 2D keypoint observation for bundle block adjustment is 528322 and number of 3D points for bundle block adjustment is 243373. The result of 3D points from 2D key point matches shown on Table 3. While the correlation between camera internal parameters determined by the bundle adjustment is ilustrated in Figure 10. Full correlation between the parameters can be fully compensated by the others, it indicates on white color. Thus, the black color indicates that the parameter is not affected by others.

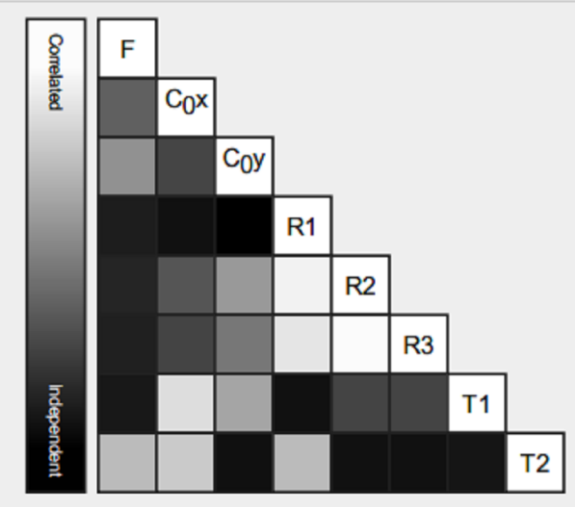

Figure 10. The correlation between camera parameters determined by bundle block adjustment

Table 3. 3D Points from 2D keypoint matches

image	Number of 3D Point Observed
In 2 images	216619
In 3 images	18817
In 4 images	4620
In 5 images	1700
In 6 images	748
In 7 images	384
In 8 images	229
In 9 images	110
In 10 images	64
In 11 images	30
In 12 images	25
In 13 images	11
In 14 images	6
In 15 images	4
In 16 images	4
In 17 images	2

Multiple 2D matching keypoints are triangulated together using the camera parameters to generate a 3D point. 3D points generated from 2-3 images are less precise than 3D points generated from a higher number of images. The result of this research is ilustrated on Figure 10. Top view of this figure computed position with a link between matching images. The darkness of the link indicates the number of matched 2D

key points between the images. Bright link indicates weak link and require manual tie points or more images.

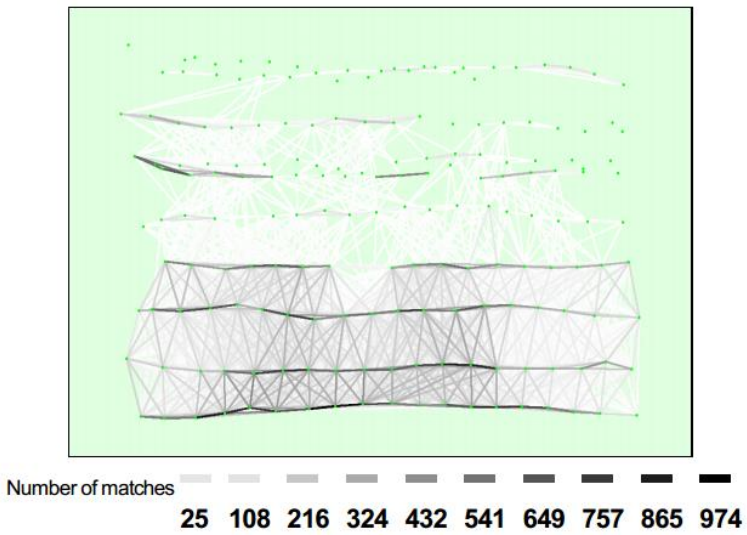

Figure 11. 3D Points from 2D keypoint matches

According to the result, multiple 2D matching keypoints are triangulated together using the camera parameters to generate a 3D point. 3D points generated from 2-3 images are less precise than 3D points generated from a higher number of images. Keypoints are points of interest on the images that can be easily recognized, in particular high contrast and interesting texture. The number of keypoints depend on size of the images and visual content. This research used camera with 14 Mega Pixels resolution. For instance, 14 Mega Pixel image will be generated between 5,000 and 50,000 keypoints per-image. If the number of keypoints is less than 1,000, the image may not have enough content to be calibrated. The number of matches will be very low if the number of keypoints is low and overlap between the images is too low.

In the 2D keypoint matches graph (Figure 11), it is possible to visualize the areas with weak matches. It might be necessary to acquire images again in these areas to increase the image overlap. The 2D keypoint matches graph (Figure 11) displays the matches between the images and the uncertainties of the relative camera positions. Each block is displayed with a different color. The uncertainty ellipses describe how precisely each image is located with respect to the other images by means of the manual and automatic tie points. Usually the ellipses in the center of the project are smaller than at the outside, as these images have more matches that bind them to the surrounding images (Luhmann et al., 2016). Large ellipses in parts of the project may indicate problems calibrating these parts of the project and typically correspond to areas with few matches.

3.3. 3D Surface Reconstruction

Surface reconstruction considered by point clouds densification (Luhmann et al., 2016; Niederheiser et al., 2016; Strecha et al., 2014). Point clouds are used in 3D modeling for generating an accurate model of real world items or scenes. If the point cloud is sparsed, the detail of the model will suffer as well as the precision of approximated geometric primitives (Forsman, 2010). Several automatic methods exist for creating 3D point clouds extracted from sets of images. They create sparse point clouds which are unevenly distributed over the objects. In this case, through the Pix4D-mapper, the process takes as input roughly geotagged images, and outputs the recomputed position of the images together with the parameters of the camera. It is presented in form of a web-based service that can automatically process up to 1000 images, is fully automated and requires no manual interaction (Küng et al., 2012).

In this result, the point clouds densification shows 6,207,780 number of 3D densified points with average density is 101.04 per m^3. From its number obtained 0.4348 value of RMS reprojection error pixels. It means the point clouds will have accuracy proportional to their scales. According to (Niederheiser et al., 2016), on the processing parameters the reprojection error in the units of tie point scale is the quantity that

is minimized during bundle adjustment, and the reprojection error in pixels. While the mean of the accuracy of tie point projections depends on the scale at which they were located.

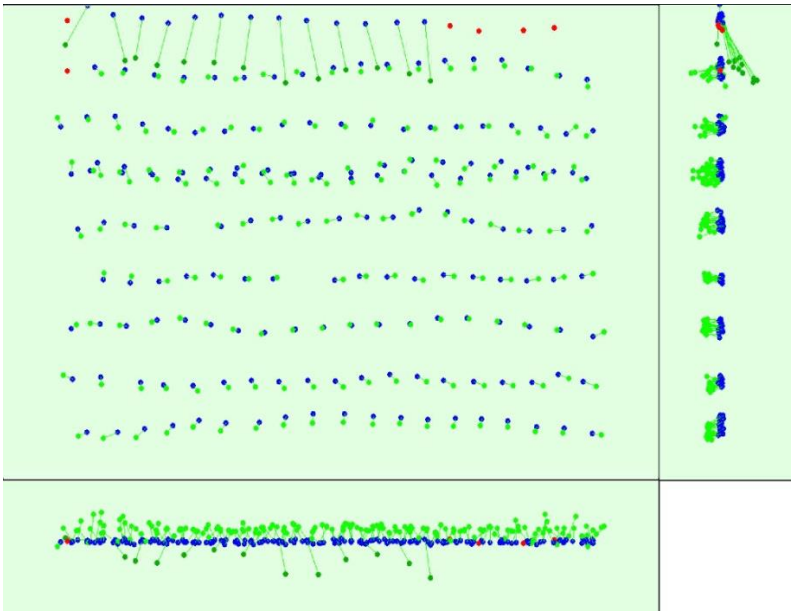

Figure 12. Computed Image - Tie Points Positions

The dense matching outputs, colored and displayed in Figure 13. The points are extremely densely sampled, which gives the illusion of texture from far away. Globally, most of the parts have been correctly reconstructed. This study area has two main difficulties for dense matching. Very repetitive texture on the surface, vegetation objects (in particular) and almost colored uniformly. Repetitive texture can lead to errors such as floating points above the terrain. The uniform color are poorly textured, and thus consistency cannot be checked and no 3D point is computed. There are much points recovered on the surface to estimate its size, however the reconstruction is too sparse to accuratly estimate objects such as a building on the surface (DSM). There is a bit of noise in the reconstruction which we visually estimate in the orders of 5 to 10 centimeters.

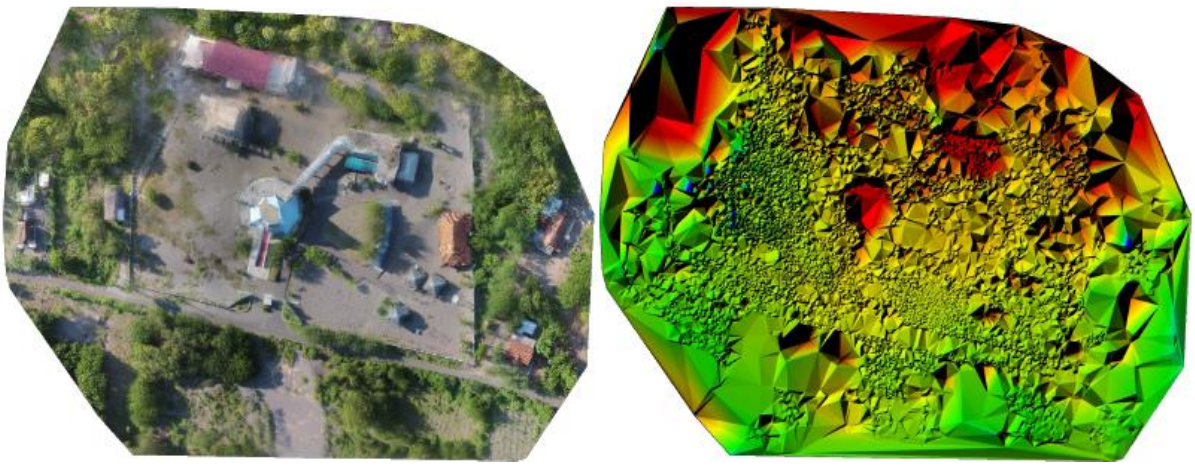

Figure 13. Orthomosaic and the corresponding sparse DSM before densification

The dense matching outputs colored and displayed in Figure 12. The surface got well reconstructed, with almost no floating pixels due to repetitive texture. The facades were a bit more problematic, due to slightly over exposed images resulting in poor photometric consistency checks in the dense matching (Küng et al., 2012). However the edges between the facades were well reconstructed, allowing the understanding of the surface's object structure (see Figure 13). Figure 14 shows the surface reconstructed.

Figure 14. Surface reconstructed (oblique view result)

3.4. Geolocation Verification

Offset between initial blue dots and computed green dots image positions as well as the offset between GCPs initial positions blue crosses and their computed positions green crosses in the top-view/XY plane, front-view/XZ plane, and side-view/YZ plane (see Figure 12). Red dots indicate disabled or uncalibrated images.

Table 4. Absolute geolocation variance

Min Error [m]	Max Error [m]	Geolocation Error X [%]	Geolocation Error Y [%]	Geolocation Error Z [%]
-	-15.00	0.00	0.00	0.00
-15.00	-12.00	0.00	0.00	0.00
-12.00	-9.00	0.00	0.00	2.99
-9.00	-6.00	0.00	0.00	15.57
-6.00	-3.00	14.97	1.20	66.47
-3.00	0.00	37.72	30.54	10.18
0.00	3.00	35.93	61.08	4.79
3.00	6.00	11.38	6.59	0.00
6.00	9.00	0.00	0.60	0.00
9.00	12.00	0.00	0.00	0.00
12.00	15.00	0.00	0.00	0.00
15.00	-	0.00	0.00	0.00
Mean		-0.221129	0.924308	-4.602879
Sigma		2.435171	1.660839	2.114381
RMS Error		2.445190	1.900718	5.065284

Min Error and Max Error represent geolocation error intervals between -1.5 and 1.5 times the maximum accuracy of all the images. Columns X, Y, Z show the percent age of images with geolocation errors within the predefined error intervals. The geolocation error is the difference between the initial and computed image positions. Despite image geolocation error might not correspond to the accuracy of the observed 3D points. Table 4 and Table 5**.** displays the percentage of geolocated and calibrated images with a geolocation error in X,Y,Z within a predefined error interval. Related to Table 4. there are ten predefined intervals between -1.5 and 1.5 times the maximum accuracy of all images. The percentage of images with an error lower than -1.5 or higher than 1.5 the accuracy values might not have been set correctly. Related to the ground sample distance (GSD), the geolocation acuracy of the model produced in this research is between 2.47 - 4.94 cm. According to this result, the model of fish-eye lenses are constructed complying with the equidistant and equisolid-angle model and more rarely the orthographic model (Schneider et al., 2009). All calculations have also been conducted assuming a central perspective projection, although this is only possible for object points with incidence angles smaller than 90°.

Table 5. Relative geolocation variance

Relative Geolocation Error	Images X [%]	Images Y [%]	Images Z [%]
[-1.**00**, 1.00]	98.80	98.80	98.20
[-2.00, 2.00]	100.00	100.00	100.00
[-3.00, 3.00]	100.00	100.00	100.00
Mean of Geolocation Accuracy	5.000000	5.000000	10.000000
Sigma of Geolocation Accuracy	0.000000	0.000000	0.000000

Related to (Schwalbe, 2005), in case of the additional calculation of the parameters of radial symmetric distortion, the mean of geolocation accuracy is identical for location error of image X, image Y, and image Z (Table 5). It related to (Schneider et al., 2009) that the differences between the fundamental geometric models are almost fully compensated by radial symmetric distortion when applying the fish-eye lenses to generated 3D models. Finally, 3D models as the result of point clouds were investigated from the resulted object coordinates of the bundle adjustment. Meanwhile, the error variance resulting some systematic effects, which are probably caused by the instabilities of the interior orientation parameters of images. Similar systematic patterns have been reported in (Schneider et al., 2009), comparing the 3D coordinates resulting from the bundle adjustment results with image variant interior orientation parameters to the reference coordinates. It has to be noted, that the remaining systematic effects might partly also be attributed to the quality of the reference coordinates.

In particular, applications of fish-eye lenses require a camera and lens calibration based on a precise geometric model to achieve accurate results. The procedures of calibration for fish-eye lenses are published for instance in (Kannala & Brandt, 2006; Schneider et al., 2009; Schwalbe, 2005). Furthermore, a calibration method like the automated-self calibration can be implemented to generate 3D model by using close-range photogrammetry technique (Luhmann et al., 2016).

4. CONCLUSION

Generating 3D surface model by using application of UAV is a new alternative for survey and mapping. Image acquisition using fish-eye lenses is a more challenging task. As they are composed of many technical parts in image processing. The automatic steps are constructed to segment the images correction in the overlaid cloud of point. The result of 3D surface model is accounted for details and location accuracy. The geometric fish-eye models can also be used to convert parts of a hemispherical image into a central perspective view to be used in photogrammetric standard software. This can be carried out by the fish-eye hemisphere and the subsequent projection of the image content on this UAV, for instance by an indirect rectification method. In the conclusion, the UAV with fish-eye lenses camera can be used to generate 3D surface model. However, images correction and calibration should be required to produce an accurate 3D surface model.

5. ACKNOWLEDGMENTS

The authors wish to acknowledge many of the UAV Team from Center for Integration and Thematic Mapping – Geospatial Information Agency (BIG) who have contributed to the images acquisition. So many thanks for Ircham Habib Anggara (BIG) and Suseno Wangsit Wijaya (BIG) as well as the improved understanding of UAS capabilities and operations in support of remote sensing and earth systems. In particular, we would like to thank Dr. Theresia Retno Wulan as the head of Parangtritis Geomaritime Science Park (PGSP). Thanks for Admin of 1st Geoplanning International Conference.

6. REFERENCES

Aber, J. S., Marzolff, I., & Ries, J. B. (2010). Small-format aerial photography: Principles, techniques and geoscience applications. *The Photogrammetric Record* (pp. 15–22). Elsevier. [Crossref]

Azmi, S. M., Ahmad, B., & Ahmad, A. (2014). Accuracy assessment of topographic mapping using UAV image integrated with satellite images. *IOP Conference Series: Earth and Environmental Science, 18*. [Crossref]

Bandara, K. R. M. U., Samarakoon, L., Shrestha, R. P., & Kamiya, Y. (2011). Automated Generation of Digital Terrain Model using Point Clouds of Digital Surface Model in Forest Area. *Remote Sensing, 3(5)*, 845–858. [Crossref]

Bemis, S. P., Micklethwaite, S., Turner, D., James, M. R., Akciz, S., Thiele, S. T., & Bangash, H. A. (2014). Ground-based and UAV-Based photogrammetry: A multi-scale, high-resolution mapping tool for structural geology and paleoseismology. *Journal of Structural Geology, 69,* 163–178. [Crossref]

Clapuyt, F., Vanacker, V., & Oost, K. Van. (2016). Reproducibility of UAV-based earth topography reconstructions based on Structure-from-Motion algorithms. *Geomorphology, 260,* 4–15. [Crossref]

Colomina, I., & Molina, P. (2014). Unmanned aerial systems for photogrammetry and remote sensing: A review. *ISPRS Journal of Photogrammetry and Remote Sensing, 92*, 79–97. [Crossref]

Cook, K. L. (2017). An evaluation of the effectiveness of low-cost UAVs and structure from motion for geomorphic change detection. *Geomorphology, 278*, 195–208. [Crossref]

Eisenbeiß, H., Zurich, E. T. H., Eisenbeiß, H., & Zürich, E. T. H. (2009). UAV photogrammetry. *Institute of Photogrammetry and Remote Sensing.* Zurich. [Crossref]

Felipe-Garc\'\ia, B., Hernández-López, D., & Lerma, J. L. (2012). Analysis of the ground sample distance on large photogrammetric surveys. *Applied Geomatics, 4(4)*, 231–244. [Crossref]

Forsman, M. (2010). Point cloud densification.

Gini, R., Pagliari, D., Passoni, D., Pinto, L., Sona, G., & Dosso, P. (2013). UAV PHOTOGRAMMETRY: BLOCK TRIANGULATION COMPARISONS. *ISPRS - International Archives of the Photogrammetry, Remote Sensing and Spatial Information Sciences, XL-1/W2*, 157–162. [Crossref]

Gularso, H., Rianasari, H., & Silalahi, F. E. S. (2015). Penggunaan foto udara format kecil menggunakan wahana udara nir-awak dalam pemetaan skala besar. *GEOMATIKA, 21(1)*, 37–44.

Gurtner, A., Greer, D. G., Glassock, R., Mejias, L., Walker, R. A., & Boles, W. W. (2009). Investigation of Fish-Eye Lenses for Small-UAV Aerial Photography. *IEEE Transactions on Geoscience and Remote Sensing, 47(3)*, 709–721. [Crossref]

Han, J., Xu, Y., Di, L., & Chen, Y. (2013). Low-cost multi-UAV technologies for contour mapping of nuclear radiation field. *Journal of Intelligent & Robotic Systems, 70(1–4)*, 401–410. [Crossref]

Kannala, J., & Brandt, S. S. (2006). A Generic Camera Model and Calibration Method for Conventional, Wide-angle and Fisheye Lens. *IEEE Transactions on Pattern Analysis and Machine Intelligence, 28(8)*, 1335–1340. [Crossref]

Kersten, T., Haering, S., & AG, S. V. (1997). Efficient automated digital aerial triangulation through customisation of a commercial photogrammetric system. *International Archives of Photogrammetry and Remote Sensing, 32(Part 3)*, 72–79.

Kršák, B., Blišťan, P., Pauliková, A., Puškárová, P., Kovanič, L., Palková, J., & Zelizňaková, V. (2016). Use of low-cost UAV photogrammetry to analyze the accuracy of a digital elevation model in a case study. *Measurement: Journal of the International Measurement Confederation, 91*, 276–287. [Crossref]

Küng, O., Strecha, C., Fua, P., Gurdan, D., Achtelik, M., Doth, K.-M., & Stumpf, J. (2012). Simplified Building Models Extraction From Ultra-Light Uav Imagery. *ISPRS - International Archives of the Photogrammetry, Remote Sensing and Spatial Information Sciences, XXXVIII-*, 217–222. [Crossref]

Luhmann, T., Fraser, C., & Maas, H.-G. (2016). Sensor modelling and camera calibration for close-range photogrammetry. *ISPRS Journal of Photogrammetry and Remote Sensing, 115*, 37–46. [Crossref]

Nex, F., & Remondino, F. (2013). UAV for 3D mapping applications: a review. *Applied Geomatics, 6(1)*, 1–15. [Crossref]

Niederheiser, R., Mokroš, M., Lange, J., Petschko, H., Prasicek, G., & Elberink, S. O. (2016). Deriving 3D Point Clouds from Terrestrial Photographs - Comparison of different sensors and software. *ISPRS - International Archives of the Photogrammetry, Remote Sensing and Spatial Information Sciences, XLI-B5*, 685–692. [Crossref]

Remondino, F., Barazzetti, L., Nex, F., Scaioni, M., & Sarazzi, D. (2012). UAV Photogrammetry for Mapping and 3D Modeling Current Status and Future Perspectives. *ISPRS - International Archives of the Photogrammetry, Remote Sensing and Spatial Information Sciences, XXXVIII-*, 25–31. [Crossref]

Schneider, D., Schwalbe, E., & Maas, H.-G. (2009). Validation of geometric models for fisheye lenses. *ISPRS Journal of Photogrammetry and Remote Sensing, 64(3)*, 259–266. [Crossref]

Schwalbe, E. (2005). Geometric modelling and calibration of fisheye lens camera systems. Institute of Photogrammetry and Remote Sensing-Dresden University of Technology, Dresden. *In Camera (Vol. XXXVI, p. Part 5/W8)*.

Strecha, C. (2011). Automated photogrammetric techniques on ultra-light UAV imagery. *Proc. of the 53rd Photogrammetric Week*, Institut Für Photogrammetrie, Universität Stuttgart, 289–294.

Strecha, C., Zoller, R., Rutishauser, S., Brot, B., Schneider-Zapp, K., Chovancova, V., … Glassey, L. (2014). Terrestrial 3D Mapping using Fisheye and Perspective Sensors.

Wang, J., & Li, C. (2008). Acquisition of UAV images and the application in 3D city modeling. *In International Symposium on Photoelectronic Detection and Imaging 2007: Image Processing (Vol. 6623*). [Crossref]